A Comparison of Nodal- and Mesh-Based Magnetic Equivalent Circuit Models

Hamza W. Derbas, *Member, IEEE*, Joshua M. Williams, *Member, IEEE*,
Andreas C. Koenig, *Member, IEEE*, and Steven D. Pekarek, *Member, IEEE*

Abstract—**The magnetic equivalent circuit (MEC) technique is a powerful analysis and design tool that combines relative accuracy with moderate computational effort. In this paper, a nodal-based MEC formulation and a mesh-based MEC formulation of a magnetic system are compared. The Newton–Raphson algorithm is used to solve the algebraic system, and to draw conclusions about the computational efficiency of the two formulations under linear and nonlinear operation. Although the two formulations exhibit similar performance under linear operating conditions, the performance of the mesh-based model is significantly better than that of the nodal-based model under nonlinear operation.**

Index Terms—**Magnetic equivalent circuit (MEC), permeance, reluctance.**

I. INTRODUCTION

MAGNETIC equivalent circuits (MECs) have been used for decades as a tool for machine analysis. Advances in computing performance have motivated a slight change in focus of MEC modeling efforts. Specifically, original papers on the technique [1]–[5] focused mainly on the analysis of saturated machine behavior. More recently, researchers have focused on its use in the design of electric machines [6]–[9]. For example, in [10], an MEC-based design program for inductors is described in which the researchers utilize evolutionary programming techniques to select 12 geometric properties of the device. A similar technique was used for induction machine design [5], [6], and wound-rotor synchronous machines [7], [8].

Increased interest in MEC as a tool for design, wherein potentially millions of model evaluations are performed as part of the design process [10], necessitates the investigation of the numerical efficiency of alternative MEC model formulations. Indeed, over the past decades, there has been considerable research on alternative model structures and solution techniques [11]. The most common formulation is one in which Kirchhoff's current law is used to establish a system of nodal equations. In such a formulation, the algebraic system is constructed using magnetic permeance to relate node potential to tube flux. Once constructed, the nonlinear algebraic system of equations has been solved using Gauss–Seidel, Newton–Raphson, or modified Newton–Raphson algorithms.

An alternative model formulation is one in which Kirchhoff's voltage law is applied to establish a system of mesh equations wherein tube flux represents the unknowns [12]. In such a formulation, the algebraic system is constructed using magnetic reluctance to relate tube flux to node MMF. Traditionally, such a formulation has received relatively minor attention. One exception is [12], [13] where a mesh analysis is used for the model derivation of a field-regulated reluctance machine.

One can argue that the mesh and nodal forms are identical. For a linear magnetic system in which saturation is neglected, such an argument is valid. However, herein it is shown that when saturation is included, a mesh formulation can yield a model that is much more efficient numerically. Specifically, it is shown that the number of iterations needed for the Newton–Raphson algorithm to converge for the mesh-based model is an order of magnitude lower than that of the nodal-based model. The difference in the number of iterations is largely due to the condition number of the Jacobian matrix, which is much smaller in the mesh formulation. Interestingly, it is also observed that in the case of the nodal formulation, an exact evaluation of the Jacobian leads to a highly ill-conditioned system.

Prior to establishing and comparing the respective formulations, it is necessary to review research that has focused on the numerical aspects of MEC formulations. There has been considerable effort focused on modeling the $B–H$ curves of magnetic material to ensure numerical stability of the respective nonlinear solution procedures [11]. Further, in [14], a state model formulation of a saturated machine was proposed in lieu of an algebraic model. If a state model formulation is used, iterative evaluation of a system of nonlinear equations is avoided, provided that the integration algorithm applied is explicit. Although the state model formulation can be advantageous, the majority of researchers continue to use an algebraic formulation. In addition, scaling of variables has been considered to prevent a subset of variables from dominating the solution effort [15]. There has also been a focus on structuring the respective MEC formulations for compatibility with the respective solution technique (Gauss–Seidel, Newton–Raphson, etc.). Finally, as MEC is analogous to electric circuit elements, it is recognized that mesh formulations have been considered for electric circuits [16]. However, the advantage of mesh formulations, and particularly for nonlinear circuits, has not been previously detailed.

II. PROBLEM FORMULATION

The result that nodal- and mesh-based MEC models have different numerical properties was first witnessed by the authors in establishing an MEC-based design program for claw-pole
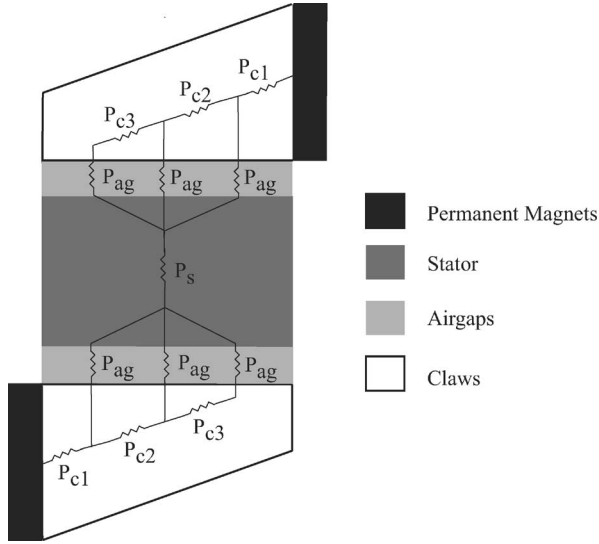
Fig. 1. Two-dimensional magnetic system.

Fig. 2. Nodal-based MEC.

alternators used in automotive applications. The claw-pole machine has a relatively complicated magnetic structure that must be modeled in three dimensions [17]. To simplify the analysis when exploring the difference between model formulations, a simplified magnetic structure was derived. Fig. 1 shows the magnetic system that provides the basis for derivations and comparisons presented herein. The geometry includes two trapezoidal core sections that are representative of the rotor structure used in claw-pole machines. Magnetic excitation is provided by two permanent magnets, located at the base of each claw. An interior core (representative of a stator) and air gap sections separate the two claws. Using this arrangement, flux travels from a claw, into the air gap, across the stator, and into the opposing claw.

A. Nodal-based MEC Model

Fig. 2 depicts the MEC that is used to represent the two-dimensional magnetic system for the respective sections (claws, air gap, and stator). Single permeance elements are used to represent the stator iron and permanent magnets. To model the spatial distribution of air gap flux, the claws are sectioned, creating a distributed permeance network. To accommodate the claw discretization, the air gap has also been divided into sections, wherein one air gap section is attached to each claw section. Additionally, the claw sections and air gap sections are symmetric about the stator permeance. Specifically, corresponding sections in opposing claws have the same permeance value and relative permeability.
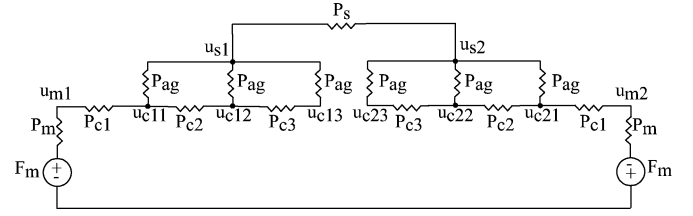
The Appendix provides derivations of the expressions for the different permeance elements, namely, permanent magnet permeance, claw section permeance, air gap permeance, and stator permeance.

To model the permeance network in Fig. 2, Kirchhoff's current law is applied at each node to create a system of nonlinear algebraic equations. In this system of equations, permanent magnet flux represents input, while nodal magnetic potentials represent outputs. Since the permanent magnets are placed at the base of the claws, only nodes u_{m1} and u_{m2} have nonzero injected flux values. For the three claw section MEC, the system has the following form:

$$\mathbf{A}_P \mathbf{u} = \boldsymbol{\varphi} \tag{1}$$

where

$$\mathbf{A}_P = \begin{bmatrix} A_{P1} & A_{P2} \\ A_{P3} & A_{P4} \end{bmatrix}. \tag{2}$$

$\mathbf{A}_{P1}$ is given by (3), shown at the bottom of this page, and

$$\mathbf{A}_{P2} = \begin{bmatrix} 0 & 0 & 0 & 0 & 0 \\ 0 & 0 & 0 & 0 & 0 \\ 0 & 0 & 0 & 0 & 0 \\ 0 & 0 & 0 & 0 & 0 \\ -P_s & 0 & 0 & 0 & 0 \end{bmatrix} \tag{4}$$

$$\mathbf{A}_{P3} = \begin{bmatrix} 0 & 0 & 0 & 0 & -P_s \\ 0 & 0 & 0 & 0 & 0 \\ 0 & 0 & 0 & 0 & 0 \\ 0 & 0 & 0 & 0 & 0 \\ 0 & 0 & 0 & 0 & 0 \end{bmatrix}. \tag{5}$$

$\mathbf{A}_{P4}$ is given by (6), shown at the bottom of the next page, and

$$\mathbf{u} = \begin{bmatrix} u_{m1} & u_{c11} & u_{c12} & u_{c13} & u_{s1} & u_{s2} & u_{c23} \\ & & & & u_{c22} & u_{c21} & u_{m2} \end{bmatrix}^T \tag{7}$$

$$\boldsymbol{\varphi} = \begin{bmatrix} F_m P_m & 0 & 0 & 0 & 0 & 0 & 0 & 0 & 0 & -F_m P_m \end{bmatrix}^T \tag{8}$$

$$F_m = H_c t_{\mathrm{mag}}. \tag{9}$$

$$\mathbf{A}_{P1} = \begin{bmatrix} P_m + P_{c1} & -P_{c1} & 0 & 0 & 0 \\ -P_{c1} & P_{\mathrm{ag}} + P_{c1} + P_{c2} & -P_{c2} & 0 & -P_{\mathrm{ag}} \\ 0 & -P_{c2} & P_{\mathrm{ag}} + P_{c2} + P_{c3} & -P_{c3} & -P_{\mathrm{ag}} \\ 0 & 0 & -P_{c3} & P_{\mathrm{ag}} + P_{c3} & -P_{\mathrm{ag}} \\ 0 & -P_{\mathrm{ag}} & -P_{\mathrm{ag}} & -P_{\mathrm{ag}} & 3P_{\mathrm{ag}} + P_s \end{bmatrix} \tag{3}$$

Fig. 3.   Mesh-based MEC.

Fig. 4. B–H curve data points for magnetic material.
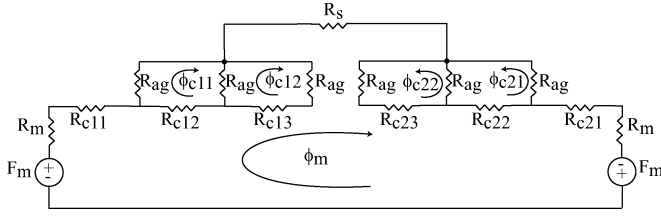
In (1)–(9), the variable P denotes permeance, u node potential (MMF), and φ flux. Furthermore, H_c and t_{mag} represent, respectively, the coercivity and thickness of the permanent magnets. It is noted here that the matrix $\mathbf{A}_P$ is a function of branch flux since it is composed of permeance elements that are dependent on branch flux.

B. Mesh-based MEC Model

The second formulation is an alternative to the previous nodal formulation. The MEC of the two-dimensional magnetic system can be represented using a reluctance network [12], [13], as shown in Fig. 3. The reluctance network maintains the same topology as the permeance network, and the claws are discretized in the same manner.
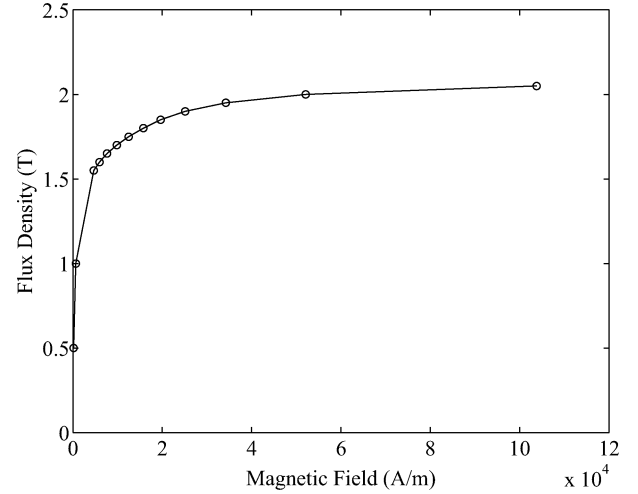
Derivations of the expressions for the different reluctance elements are provided in the Appendix.

By applying Kirchhoff's voltage law to each of the defined loops, a system of nonlinear algebraic equations can be developed for the reluctance network in Fig. 3. In this system of equations, loop voltages are inputs, while mesh currents are outputs. Again, since the permanent magnets are placed at the base of the claws, only the mesh with current Φ_m has nonzero loop voltage. For the three claw section MEC, the system has the following form:

$$\mathbf{A}_R \varphi = \mathbf{F} \tag{10}$$

where $\mathbf{A}_R$ is given by (11), shown at the bottom of this page

$$R_M = 2R_m + 2R_{\mathrm{ag}} + R_s + R_{c11} + R_{c12}$$
$$+ R_{c13} + R_{c21} + R_{c22} + R_{c23} \tag{12}$$

$$\varphi = \begin{bmatrix} \phi_m & \phi_{c11} & \phi_{c12} & \phi_{c22} & \phi_{c21} \end{bmatrix}^T \tag{13}$$

$$\mathbf{F} = \begin{bmatrix} 2F_m & 0 & 0 & 0 & 0 \end{bmatrix}^T \tag{14}$$

$$F_m = H_c t_{\mathrm{mag}}. \tag{15}$$

In (10)–(14), R is used to represent reluctance. It is noted here that the matrix $\mathbf{A}_R$ is also a function of branch flux since it is composed of reluctance elements that are dependent on branch flux. Furthermore, H_c and t_{mag} represent, respectively, the coercivity and thickness of the permanent magnets.

C. B–H Model

For both formulations, a set of data points was used to derive the B–H curve for the iron material (stator and claws). This curve was then used to construct the μ–B curve through a piecewise combination of a linear function, a quadratic spline, and a unity constant. Figs. 4 and 5 depict the B–H curve and μ–B curve, respectively.

$$\mathbf{A}_{P4} = \begin{bmatrix} 3P_{\mathrm{ag}} + P_s & -P_{\mathrm{ag}} & -P_{\mathrm{ag}} & -P_{\mathrm{ag}} & 0 \\ -P_{\mathrm{ag}} & P_{\mathrm{ag}} + P_{c3} & -P_{c3} & 0 & 0 \\ -P_{\mathrm{ag}} & -P_{c3} & P_{\mathrm{ag}} + P_{c2} + P_{c3} & -P_{c2} & 0 \\ -P_{\mathrm{ag}} & 0 & -P_{c2} & P_{\mathrm{ag}} + P_{c1} + P_{c2} & -P_{c1} \\ 0 & 0 & 0 & -P_{c1} & P_m + P_{c1} \end{bmatrix} \tag{6}$$

$$\mathbf{A}_R = \begin{bmatrix} R_M & -R_{c12} & -R_{c13} - R_{\mathrm{ag}} & R_{c23} + R_{\mathrm{ag}} & R_{c22} \\ -R_{c12} & R_{c12} + 2R_{\mathrm{ag}} & -R_{\mathrm{ag}} & 0 & 0 \\ -R_{c13} - R_{\mathrm{ag}} & -R_{\mathrm{ag}} & R_{c13} + 2R_{\mathrm{ag}} & 0 & 0 \\ R_{c23} + R_{\mathrm{ag}} & 0 & 0 & R_{c23} + 2R_{\mathrm{ag}} & -R_{\mathrm{ag}} \\ R_{c22} & 0 & 0 & -R_{\mathrm{ag}} & R_{c22} + 2R_{\mathrm{ag}} \end{bmatrix} \tag{11}$$
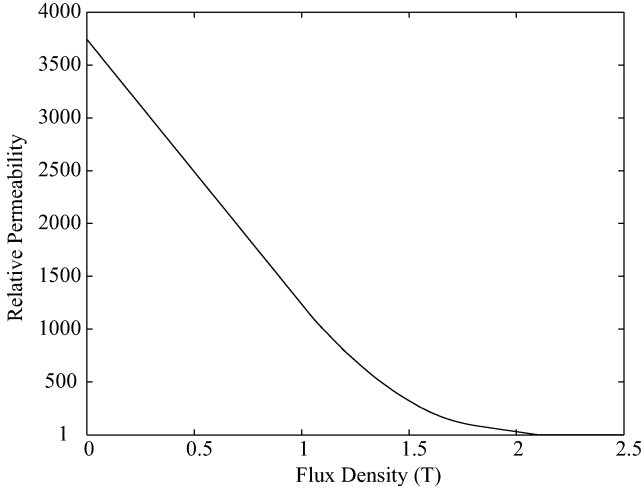
Fig. 5. μ–B curve for magnetic material.

III. ANALYTICAL SOLUTION OF MEC SYSTEMS

Several numerical methods can be used to solve systems of nonlinear equations. Due to its numerical stability and convergence properties, the Newton–Raphson method was elected to be used for both the nodal- and mesh-based formulations.

A. Solution of the Nodal-based MEC System

The system of equations in (1) is rearranged to be in the form:

$$f(\mathbf{u}) = \mathbf{A}_P \mathbf{u} - \boldsymbol{\varphi} = 0. \tag{16}$$

To illustrate this rearrangement, the first equation in this set is presented

$$f_1(\mathbf{u}) = (P_m + P_{c1}) u_{m1} - P_{c1} u_{c11} - F_m P_m = 0. \tag{17}$$

In this equation, P_{c1} is the only flux dependent permeance. This dependency lies in the value of relative permeability, which is obtained from the B–H curve, and is updated every iteration. The flux through this permeance element is:

$$\Phi_{c1} = P_{c1} (u_{m1} - u_{c11}) \tag{18}$$

and the corresponding flux density in this permeance element is:

$$B_{c1} = \frac{\Phi_{c1}}{A_{c1}} \tag{19}$$

where A_{c1} represents the cross-sectional area for the flux tube of the respective claw section. In the claw-pole machine, the claw sections do not have constant cross-sectional area. Thus, this area is "chosen" by the system analyst. In this research, the area two-thirds from the longer side of each claw section was selected. This selection has yielded reasonable results as compared to finite-element (FE) based models [18].

Next, the Jacobian matrix $\mathbf{J}$ is constructed. Again, to illustrate, the first entry of the matrix $\mathbf{J}$ is presented

$$J_{11} = \frac{\partial f_1}{\partial u_{m1}} = (P_m + P_{c1}) + \frac{\partial P_{c1}}{\partial u_{m1}} (u_{m1} - u_{c11}). \tag{20}$$

The first term in J_{11} is clearly the first entry of A_P. Applying the chain rule to resolve the second term in J_{11}, the following expression is obtained:

$$\frac{\partial P_{c1}}{\partial u_{m1}} = \frac{\partial P_{c1}}{\partial \mu_{rc1}} \frac{\partial \mu_{rc1}}{\partial B_{c1}} \frac{\partial B_{c1}}{\partial \Phi_{c1}} \frac{\partial \Phi_{c1}}{\partial u_{m1}}. \tag{21}$$

Referring to the permeance expression in (62) (see Appendix), the first term in the previous equation becomes:

$$\frac{\partial P_{c1}}{\partial \mu_{rc1}} = \frac{\mu_0 N (l_1 - l_2)}{l_{\text{claw}} \ln (l_1/l_2)} = \frac{P_{c1}}{\mu_{rc1}}. \tag{22}$$

This term will be denoted by α. The second term, denoted by β, is obtained from the B–H curve. The third term, denoted by γ, is simply:

$$\frac{\partial B_{c1}}{\partial \Phi_{c1}} = \frac{1}{A_{c1}}. \tag{23}$$

At first glance, the final term seems to suggest that $\partial P_{c1}/\partial u_{m1}$ cannot be resolved into a closed form since:

$$\frac{\partial \Phi_{c1}}{\partial u_{m1}} = \frac{\partial P_{c1}}{\partial u_{m1}} (u_{m1} - u_{c11}) + P_{c1}. \tag{24}$$

However, by substituting (24) into (21), arranging terms such that $\partial P_{c1}/\partial u_{m1}$ is on the left-hand side and all other terms are on the right-hand side, then dividing through, one can solve for $\partial P_{c1}/\partial u_{m1}$ to obtain the following:

$$\frac{\partial P_{c1}}{\partial u_{m1}} = \frac{\alpha\beta\gamma P_{c1}}{1 - \alpha\beta\gamma (u_{m1} - u_{c11})}. \tag{25}$$

This process can be repeated for all the partial derivative terms in the entries of J.

B. Solution of the Mesh-based MEC System

In a similar manner to the nodal-based system, the system of equations in (10) is rearranged to be in the form:

$$g(\boldsymbol{\varphi}) = \mathbf{A}_R \boldsymbol{\varphi} - \mathbf{F} = 0. \tag{26}$$

To illustrate this rearrangement, the first equation in this set is presented

$$g_1(\boldsymbol{\varphi}) = R_M \phi_m - R_{c12}\phi_{c11} - (R_{c13} + R_{\text{ag}}) \phi_{c12}$$
$$+ (R_{c23} + R_{\text{ag}}) \phi_{c22} + R_{c22}\phi_{c21} - 2F_m = 0 \tag{27}$$

$$R_M = 2R_m + 2R_{\text{ag}} + R_s + R_{c11} + R_{c12} + R_{c13}$$
$$+ R_{c21} + R_{c22} + R_{c23}. \tag{28}$$

In this equation, $R_{c11}, R_{c12}, R_{c13}, R_{c21}, R_{c22}$, and R_{c23} are flux dependent reluctances. The flux in these elements is:

$$\Phi_{c11} = \phi_m$$
$$\Phi_{c12} = \phi_{c11} - \phi_m$$
$$\Phi_{c13} = \phi_{c12} - \phi_m$$
$$\Phi_{c21} = \phi_m$$
$$\Phi_{c22} = \phi_{c21} + \phi_m$$
$$\Phi_{c23} = \phi_{c22} + \phi_m. \tag{29}$$

Next, the Jacobian matrix $\mathbf{J}$ is constructed. The first entry of this matrix is:

$$
\begin{aligned}
J_{11} &= R_M + \frac{\partial R_M}{\partial \phi_m}\phi_m - \frac{\partial R_{c12}}{\partial \phi_m}\phi_{c11} + \frac{\partial R_{c13}}{\partial \phi_m}\phi_{c12} \\
&\quad + \frac{\partial R_{c23}}{\partial \phi_m}\phi_{c22} + \frac{\partial R_{c22}}{\partial \phi_m}\phi_{c21} \\
&= R_M + \frac{\partial R_{c11}}{\partial \phi_m}\phi_m + \frac{\partial R_{c21}}{\partial \phi_m}\phi_m + \frac{\partial R_{c12}}{\partial \phi_m}\left(\phi_m - \phi_{c11}\right) \\
&\quad + \frac{\partial R_{c22}}{\partial \phi_m}\left(\phi_m + \phi_{c21}\right) \\
&\quad + \frac{\partial R_{c13}}{\partial \phi_m}\left(\phi_m - \phi_{c12}\right) + \frac{\partial R_{c23}}{\partial \phi_m}\left(\phi_m + \phi_{c22}\right).
\end{aligned}
\tag{30}
$$

The first term of this entry is exactly the first entry of the matrix $\mathbf{A}_R$. All the other terms are produced by the flux dependent reluctances. All these partial derivative terms need to be resolved as follows:

$$
\frac{\partial R_{c12}}{\partial \phi_m} = \frac{\partial R_{c12}}{\partial \mu_{rc12}}\frac{\partial \mu_{rc12}}{\partial B_{c12}}\frac{\partial B_{c12}}{\partial \Phi_{c12}}\frac{\partial \Phi_{c12}}{\partial \phi_m}.
\tag{31}
$$

Referring to (19), (29), and (61), the following expressions are obtained:

$$
R_{c12} = \frac{l_{\text{claw}}}{\mu_0 \mu_{rc12} N \left(l_1 - l_2\right)} \ln\left(\frac{l_1}{l_2}\right)
\tag{32}
$$

$$
\Phi_{c12} = \phi_{c11} - \phi_m
\tag{33}
$$

$$
B_{c12} = \frac{\Phi_{c12}}{A_{c12}}
\tag{34}
$$

where A_{c12} is the cross-sectional area for that claw section. Furthermore

$$
\frac{\partial R_{c12}}{\partial \mu_{rc12}} = -\frac{1}{\mu_{rc12}}R_{c12}
\tag{35}
$$

$$
\frac{\partial B_{c12}}{\partial \Phi_{c12}} = \frac{1}{A_{c12}}
\tag{36}
$$

$$
\frac{\partial \Phi_{c12}}{\partial \phi_m} = -1.
\tag{37}
$$

Therefore

$$
\frac{\partial R_{c12}}{\partial \phi_m} = \frac{R_{c12}}{\mu_{rc12}A_{c12}}\frac{\partial \mu_{rc12}}{\partial B_{c12}}.
\tag{38}
$$

The term $\partial \mu_{rc12}/\partial B_{c12}$ is obtained from the B–H curve; hence, these results allow one to analytically compute the Jacobian matrix with relative ease, which was not possible with the nodal-based model. The Jacobian matrix $\mathbf{J}$ for the system has the following form:

$$
\mathbf{J} = \mathbf{A}_R + \mathbf{pA}_R
\tag{39}
$$

where $\mathbf{pA}_R$ is the matrix containing all the resolved partial derivative terms. Considering three claw sections, this matrix has the following entries:

$$
\mathbf{pA}_R = \begin{bmatrix}
pA_{11} & pA_{12} & pA_{13} & pA_{14} & pA_{15} \\
pA_{21} & pA_{22} & 0 & 0 & 0 \\
pA_{31} & 0 & pA_{33} & 0 & 0 \\
pA_{41} & 0 & 0 & pA_{44} & 0 \\
pA_{51} & 0 & 0 & 0 & pA_{55}
\end{bmatrix}
\tag{40}
$$

$$
\begin{aligned}
pA_{11} &= \frac{\partial R_{c11}}{\partial \phi_m}\phi_m + \frac{\partial R_{c21}}{\partial \phi_m}\phi_m + \frac{\partial R_{c12}}{\partial \phi_m}\left(\phi_m - \phi_{c11}\right) \\
&\quad + \frac{\partial R_{c22}}{\partial \phi_m}\left(\phi_m + \phi_{c21}\right) + \frac{\partial R_{c13}}{\partial \phi_m}\left(\phi_m - \phi_{c12}\right) \\
&\quad + \frac{\partial R_{c23}}{\partial \phi_m}\left(\phi_m + \phi_{c22}\right)
\end{aligned}
\tag{41}
$$

$$
pA_{12} = \frac{\partial R_{c12}}{\partial \phi_{c11}}\left(\phi_m - \phi_{c11}\right)
\tag{42}
$$

$$
pA_{13} = \frac{\partial R_{c13}}{\partial \phi_{c12}}\left(\phi_m - \phi_{c12}\right)
\tag{43}
$$

$$
pA_{14} = \frac{\partial R_{c23}}{\partial \phi_{c22}}\left(\phi_m + \phi_{c22}\right)
\tag{44}
$$

$$
pA_{15} = \frac{\partial R_{c22}}{\partial \phi_{c21}}\left(\phi_m + \phi_{c21}\right)
\tag{45}
$$

$$
pA_{21} = \frac{\partial R_{c12}}{\partial \phi_m}\left(-\phi_m + \phi_{c11}\right)
\tag{46}
$$

$$
pA_{22} = \frac{\partial R_{c12}}{\partial \phi_{c11}}\left(-\phi_m + \phi_{c11}\right)
\tag{47}
$$

$$
pA_{31} = \frac{\partial R_{c13}}{\partial \phi_m}\left(-\phi_m + \phi_{c12}\right)
\tag{48}
$$

$$
pA_{33} = \frac{\partial R_{c13}}{\partial \phi_{c12}}\left(-\phi_m + \phi_{c12}\right)
\tag{49}
$$

$$
pA_{41} = \frac{\partial R_{c23}}{\partial \phi_m}\left(\phi_m + \phi_{c22}\right)
\tag{50}
$$

$$
pA_{44} = \frac{\partial R_{c23}}{\partial \phi_{c22}}\left(\phi_m + \phi_{c22}\right)
\tag{51}
$$

$$
pA_{51} = \frac{\partial R_{c22}}{\partial \phi_m}\left(\phi_m + \phi_{c21}\right)
\tag{52}
$$

$$
pA_{55} = \frac{\partial R_{c22}}{\partial \phi_{c21}}\left(\phi_m + \phi_{c21}\right).
\tag{53}
$$

This completes all the preliminaries for implementing the Newton–Raphson iterative method.

IV. MODELING RESULTS

Studies were performed to evaluate the convergence rate and air gap flux density results for both circuit formulations. The coercivity of the permanent magnets was varied to mimic different flux values in the nonlinear magnetic region.

For the nodal-based network, two different approaches were used to simulate the system. The first was based on the analytically obtained Jacobian, using expressions shown in (20)
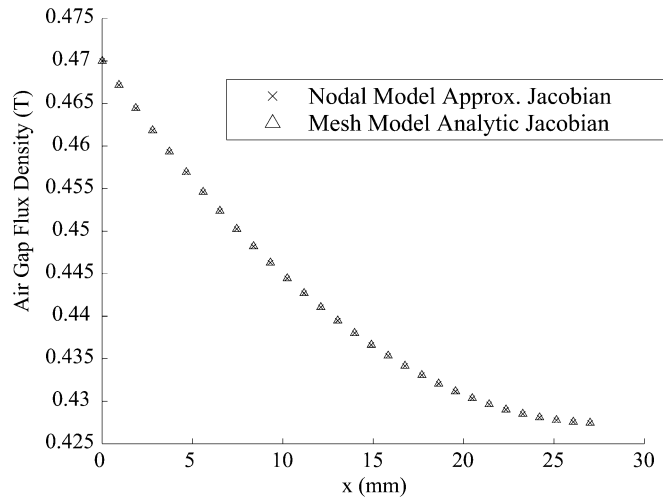
Fig. 6. Air gap flux density for a coercivity of 10^5 A/m.

TABLE I
CONVERGENCE DATA FOR $H_c = 10^5$ A/m

Implementation	Convergence
Nodal Model Approx. Jacobian	3 iterations
Nodal Model Analytic Jacobian	3 iterations
Mesh Model Analytic Jacobian	4 iterations

and (25). Through evaluation, it was found that the analytically obtained Jacobian yielded convergence issues, and so, an alternative approximation $\mathbf{J} = \mathbf{A}_P$ was also applied. In the mesh-based formulation, the analytically obtained Jacobian was used for all studies.

Fig. 6 depicts the air gap flux density curves for a case in which the permanent magnet coercivity was set to 10^5 A/m. Thirty sections were used to model the flux distribution in the rotor claw. A tolerance constraint of 10^{-6} was used as a basis for convergence. The results were obtained from the approximate and analytically obtained Jacobian approaches for the nodal-based MEC model, as well as the analytically obtained Jacobian approach for the mesh-based MEC model. As seen in Fig. 6, all three approaches produce the same result.

Table I presents the convergence data for the different approaches.

Fig. 7 depicts the air gap flux density curves for a case in which the permanent magnet coercivity was increased to 8×10^5 A/m. For this case, the nodal model that uses an analytically obtained Jacobian fails to converge to a reasonable solution. The remaining two MEC implementations converge to the same solution which is plotted in Fig. 7.
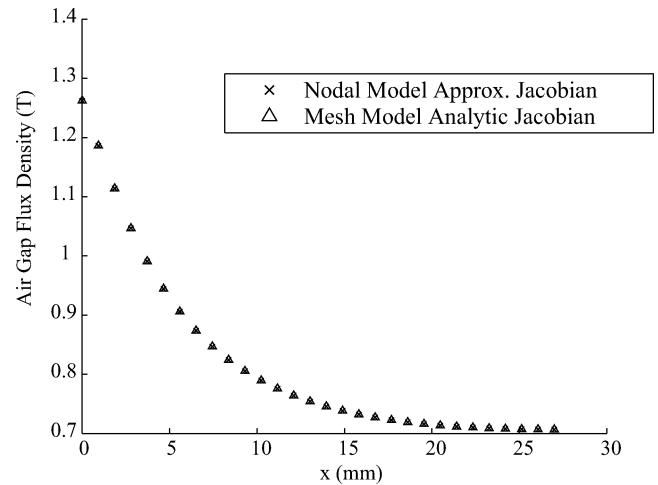
Table II presents the convergence/termination data for the different approaches.

Fig. 8 depicts the air gap flux density curves for a case in which the permanent magnet coercivity was increased to 16×10^5 A/m. As in the previous study, the nodal-based model that utilizes an analytic Jacobian fails to converge to a reasonable solution. As shown in Fig. 8, the remaining two MEC implementations converge to the same solution.

Furthermore, Fig. 9 depicts the flux density curves along the claw for both MEC implementations. Again, both imple-
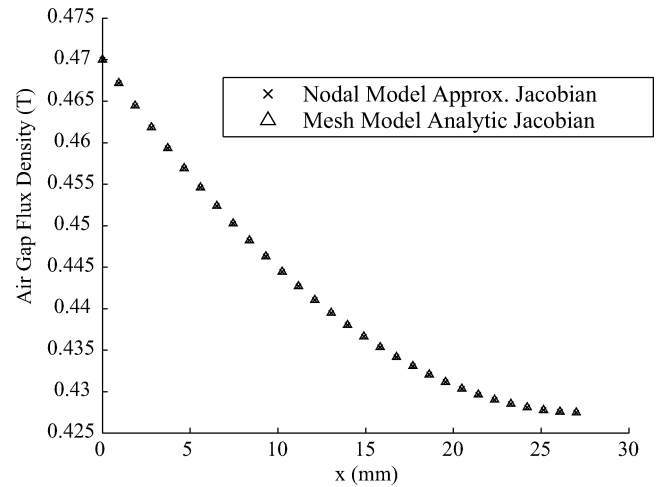
Fig. 7. Air gap flux density for a coercivity of 8×10^5 A/m.

TABLE II
CONVERGENCE DATA FOR $H_c = 8 \times 10^5$ A/m

Implementation	Convergence
Nodal Model Approx. Jacobian	5 iterations
Nodal Model Analytic Jacobian	Did not converge
Mesh Model Analytic Jacobian	5 iterations

Fig. 8. Air gap flux density for a coercivity of 16×10^5 A/m.

mentations converge to the same solution. The high levels of flux density verify that the system is operating under nonlinear/saturation conditions.

Table III presents the convergence/termination data for the different approaches.

Operating further into saturation yields an increasing difference between the nodal and mesh model iteration numbers. Indeed, Table IV illustrates the convergence data for a case in which the coercivity is increased to 18×10^5 A/m.

V. INTERPRETATION OF RESULTS

The results in the previous section clearly show that there is a significant advantage to using the mesh-based model. Interpreting this result requires investigating the solution methodology,
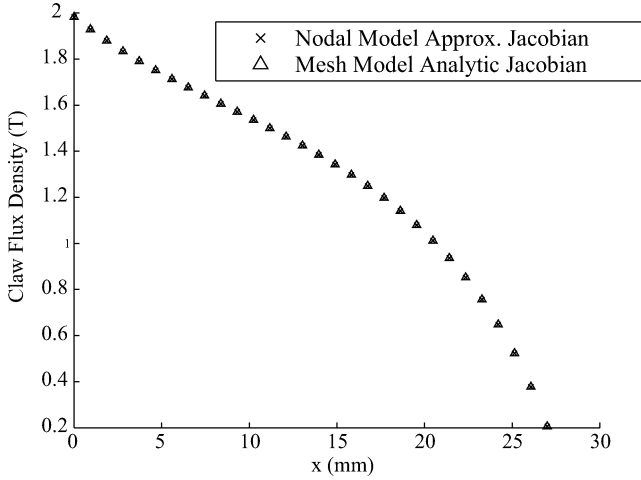
Fig. 9. Claw flux density for a coercivity of 16×10^5 A/m.

Fig. 10. Components of the magnetic system.

TABLE III
CONVERGENCE DATA FOR $H_c = 16 \times 10^5$ A/m

Implementation	Convergence
Nodal Model Approx. Jacobian	53 iterations
Nodal Model Analytic Jacobian	Did not converge
Mesh Model Analytic Jacobian	6 iterations

TABLE IV
CONVERGENCE DATA FOR $H_c = 18 \times 10^5$ A/m

Implementation	Convergence
Nodal Model Approx. Jacobian	95 iterations
Nodal Model Analytic Jacobian	Did not converge
Mesh Model Analytic Jacobian	7 iterations

TABLE V
CONDITION NUMBERS FOR THE MEC IMPLEMENTATIONS

Implementation	Condition Number
Nodal Model Approx. Jacobian	$\sim 2 \times 10^5$
Nodal Model Analytic Jacobian	$\sim 2 \times 10^8$
Mesh Model Analytic Jacobian	~ 500

Fig. 11. Single claw section.

namely, the Newton–Raphson method. For a single variable, the Newton–Raphson method takes on the following form:

$$x_{n+1} = x_n - \frac{f(x_n)}{f'(x_n)}. \tag{54}$$

For values of $f'(x_n)$ close to zero, the method fails to converge. For multiple variables, the method has the following form:

$$\mathbf{x_{n+1}} = \mathbf{x_n} - [J(\mathbf{x_n})]^{-1} \mathbf{f}(\mathbf{x_n}). \tag{55}$$

For ill-conditioned Jacobian matrices $J(\mathbf{x_n})$, the method fails to converge [19]. Table V shows general trends for the condition numbers of the Jacobian matrices for the three different implementations.

The information in the table verifies the results obtained in the previous section. It is clear that the mesh-based approach is the most favorable, as condition numbers are relatively small as compared to the other approaches, leading to significantly faster convergence rates.
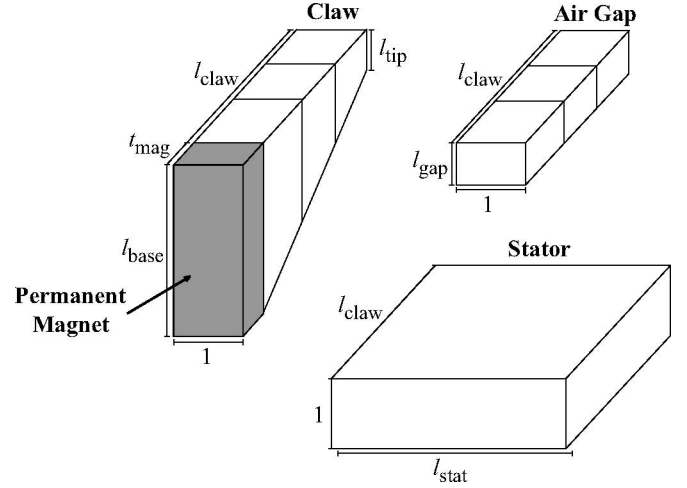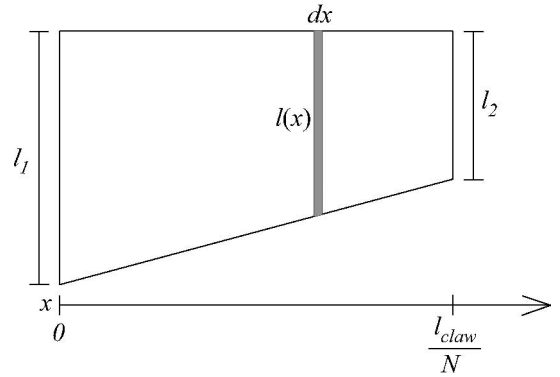
In an attempt to overcome the problem of ill-conditioned Jacobian matrices, scaling of the vector variable $\mathbf{u}$ in (1) was investigated. The ill conditioning is caused by the value of the air gap permeance P_{ag}, which is 3 orders of magnitude smaller than the other permeances. The term P_{ag} appears in a number of symmetric nondiagonal entries of the matrix $\mathbf{A}_P$. This renders scaling useless, as scaling one variable that multiplies P_{ag} requires scaling other permeance terms in $\mathbf{A}_P$, eventually leading to another ill-conditioned matrix.

VI. CONCLUSION

In this paper, two MEC formulations of a magnetic system representative of a claw-pole structure are considered. For both formulations, the Jacobian of the algebraic system was analytically obtained for use in the Newton–Raphson algorithm. Under linear operating conditions, both formulations have similar performance; however, under nonlinear operating conditions, the computational performance of the mesh-based MEC model far exceeds that of the nodal-based MEC model. The difference in performance is due to the difference in the condition number of the Jacobian matrices of the respective models.

APPENDIX

Figure 10 depicts the shapes of all the components of the magnetic system. It is noted that in flattening the three-dimensional model, unity thickness is assumed for all components.

For the permanent magnet, the cross-sectional area is fixed; hence,

$$P_m = \frac{\mu_0 \mu_{r\,\mathrm{mag}} l_{\mathrm{mag}}}{t_{\mathrm{mag}}} \tag{56}$$

$$R_m = \frac{t_{\mathrm{mag}}}{\mu_0 \mu_{r\,\mathrm{mag}} l_{\mathrm{mag}}} \tag{57}$$

where μ_{mag} is the relative permeability of the permanent magnet.

Next, each claw is divided into N sections. Since claw cross-sectional area is position dependent, it is convenient to first determine the reluctance of a claw section.

For claw section i depicted in Fig. 11, the expression for length (and hence area) as a function of position is:

$$l(z) = \frac{N(l_2 - l_1)}{l_{\mathrm{claw}}} z + l_1. \tag{58}$$

The differential form of reluctance thus becomes:

$$dR_{ci} = \frac{dz}{\mu_0 \mu_{rci} \left[(N(l_2 - l_1)/l_{\mathrm{claw}}) z + l_1 \right]} \tag{59}$$

which implies that

$$R_{ci} = \int dR_{ci} = \int_{l_1}^{l_2} \frac{dz}{\mu_0 \mu_{rci} \left[(N(l_2 - l_1)/l_{\mathrm{claw}}) z + l_1 \right]}. \tag{60}$$

Therefore

$$R_{ci} = \frac{l_{\mathrm{claw}}}{\mu_0 \mu_{rci} N(l_1 - l_2)} \ln\left(\frac{l_1}{l_2}\right) \tag{61}$$

$$P_{ci} = \frac{\mu_0 \mu_{rci} N(l_1 - l_2)}{l_{\mathrm{claw}} \ln(l_1/l_2)} \tag{62}$$

where μ_{rci} is the relative permeability of claw section i.

The remaining two components have constant cross-sectional areas. The air gaps are discretized in the same manner as the claws and hence:

$$P_{\mathrm{ag}} = \frac{\mu_0 l_{\mathrm{claw}}}{N l_{\mathrm{gap}}} \tag{63}$$

$$R_{\mathrm{ag}} = \frac{N l_{\mathrm{gap}}}{\mu_0 l_{\mathrm{claw}}}. \tag{64}$$

The stator permeance and reluctance can be expressed as follows:

$$P_s = \frac{\mu_0 \mu_s l_{\mathrm{claw}}}{l_{\mathrm{stat}}} \tag{65}$$

$$R_s = \frac{l_{\mathrm{stat}}}{\mu_0 \mu_s l_{\mathrm{claw}}} \tag{66}$$

where μ_s is the relative permeability of the stator.

REFERENCES

[1] G. R. Slemon, "Equivalent circuits for transformers and machines including non-linear effects," *Proc. IEE*, vol. 100, part iv, pp. 129–143, Jul. 1953.

[2] J. Fiennes, "New approach to general theory of electrical machines using magnetic equivalent circuits," *Proc. IEE*, vol. 120, pp. 94–104, Jan. 1973.

[3] V. Ostović, "A method for evaluation of transient and steady state performance in saturated squirrel cage induction machines," *IEEE Trans. Energy Convers.*, vol. EC-1, no. 3, pp. 190–197, Sep. 1986.

[4] V. Ostović, "Magnetic equivalent circuit presentation of electric machines," *Electr. Mach. Power Syst.*, vol. 12, pp. 407–432, Jun. 1987.

[5] S. D. Sudhoff, B. T. Kuhn, K. A. Corzine, and B. T. Branecky, "Magnetic equivalent circuit modeling of induction motors," *IEEE Trans. Energy Convers.*, vol. 22, no. 2, pp. 259–270, Jun. 2007.

[6] J. Perho, "Reluctance network for analyzing induction machines," *Acta Polytech. Scandinavica, Electr. Eng. Series*, vol. 110, pp. 1–147, Dec. 2002.

[7] G. R. Slemon, "An equivalent circuit approach to analysis of synchronous machines with saliency and saturation," *IEEE Trans. Energy Convers.*, vol. 5, no. 3, pp. 538–545, Sep. 1990.

[8] Y. Xiao, G. R. Slemon, and M. R. Iravani, "Implementation of an equivalent circuit approach to the analysis of synchronous machines," *IEEE Trans. Energy Convers.*, vol. 9, no. 4, pp. 717–723, Dec. 1994.

[9] C. B. Rasmussen and E. Ritchie, "A magnetic equivalent circuit approach for predicting PM motor performance," in *Proc. Rec. Ind. Appl. Conf.*, New Orleans, LA, Oct. 5–9, 1997, vol. 1, pp. 10–17.

[10] J. Cale and S. D. Sudhoff, "EI core inductor designs using population-based design algorithms," in *Proc. 22nd Ann. IEEE Appl. Power Electron. Conf., APEC 2007*, Anaheim, CA, Feb.–Mar., pp. 1062–1069.

[11] V. Ostović, *Dynamics of Saturated Electric Machines*. New York: Springer-Verlag, 1989.

[12] J. D. Law, T. J. Busch, and T. A. Lipo, "Magnetic circuit modeling of the field regulated reluctance machine. Part I: Model development," *IEEE Trans. Energy Convers.*, vol. 11, no. 1, pp. 49–55, Mar. 1996.

[13] T. J. Busch, J. D. Law, and T. A. Lipo, "Magnetic circuit modeling of the field regulated reluctance machine. Part II: Saturation modeling and results," *IEEE Trans. Energy Convers.*, vol. 11, no. 1, pp. 56–61, Mar. 1996.

[14] V. Ostović, "A novel method for evaluation of transient states in saturated electric machines," *IEEE Trans. Ind. Appl.*, vol. 25, no. 1, pp. 96–100, Jan.–Feb. 1989.

[15] M. Amrhein, "Induction machine performance improvements—Design-oriented approaches," Ph.D. dissertation, Dept. Electr. Comput. Eng., Univ. Illinois Urbana-Champaign, Urbana, IL, Apr. 2007.

[16] P. M. Lin, *Symbolic Network Analysis*. New York: Elsevier, 1991.

[17] V. Ostović, J. M. Miller, V. Garg, R. Schultz, and S. Swales, "A magnetic equivalent circuit based performance computation of a Lundell alternator," *IEEE Trans. Ind. Appl.*, vol. 35, no. 4, pp. 825–830, Jul./Aug. 1999.

[18] J. M. Williams, "Modeling and analysis of electric machines with asymmetric rotor poles using a reluctance based, magnetic equivalent circuit," Ph.D. dissertation, Dept. Electr. Comput. Eng., Univ. Missouri-Rolla, Rolla, MO, 2004.

[19] S. G. Nash and A. Sofer, *Linear and Nonlinear Programming*. New York: McGraw-Hill, 1996.

Hamza W. Derbas (S'01–M'08) received the B.S. degree from the American University of Beirut, Beirut, Lebanon, in 2005, and the M.S. degree from Purdue University, West Lafayette, IN, both in electrical engineering.

As a graduate student, his research interests included control systems, electric machinery, and linear algebra. He is currently a Project Engineer with FEV Inc., Auburn Hills, MI. His current research interests include hardware and software controls design for electric and hybrid electric vehicles, as well as electric drive systems.

Joshua M. Willaims (M'99) received the B.S., M.S., and Ph.D. degrees in electrical engineering from the University of Missouri-Rolla, Rolla, MO, in 1999, 2001, and 2004, respectively.

As a graduate student, he was National Science Foundation Integrative Graduate Education and Research Traineeship (IGERT) Fellow. He is currently a Research Engineer with Caterpillar, Peoria, IL. His current research interests include design and analysis of electric machinery and drive systems.

Andreas C. Koenig (M'99) received the B.S. and M.S. degrees in electrical engineering from the University of Missouri-Rolla, Rolla, MO, in 2001 and 2003, respectively.

During 2003–2004, he was a Research Assistant at the Institute for Power Electronics and Electrical Drives, Rheinisch-Westfälische Technische Hochschule Aachen (RWTH) University, Aachen, Germany. He is currently a National Science Foundation Graduate Research Fellow at Purdue University, West Lafayette, IN. His current research interests include hardware design, numerical analysis, and automated control of power electronic systems and electric machinery.

Steven D. Pekarek (S'89–M'96) received the Ph.D. degree in electrical engineering from Purdue University, West Lafayette, IN, in 1996.

During 1997–2004, he was an Assistant (Associate) Professor of Electrical and Computer Engineering at the University of Missouri-Rolla. He is currently a Professor of Electrical and Computer Engineering at Purdue University. As a faculty member, he has been the Principal Investigator on a number of successful research programs including projects for the Navy, Air Force, Ford Motor Company, Motorola, and Delphi. His current research interests include analysis and design of electric machines and power electronics for finite inertia power and propulsion systems.

Dr. Pekarek is an active member of the IEEE Power Engineering Society, the Society of Automotive Engineers, and the IEEE Power Electronics Society. He was the Technical Co-Chair of the 2005 IEEE International Electric Machines and Drives Conference, the Technical Chair of the 2007 IEEE Applied Power Electronics Conference, and the Chair of the 2008 IEEE Applied Power Electronics Conference.